

First hard X-ray detection of the non-thermal emission around the Arches cluster: morphology and spectral studies with *NuSTAR*

Roman A. Krivonos¹, John A. Tomsick¹, Franz E. Bauer^{2,3}, Frederick K. Baganoff⁴,
 Nicolas M. Barriere¹, Arash Bodaghee¹, Steven E. Boggs¹, Finn E. Christensen⁵,
 William W. Craig^{6,1}, Brian W. Grefenstette⁷, Charles J. Hailey⁸, Fiona A. Harrison⁷,
 JaeSub Hong⁹, Kristin K. Madsen⁷, Kaya Mori⁸, Melania Nynka⁸, Daniel Stern¹⁰,
 William W. Zhang¹¹

ABSTRACT

The Arches cluster is a young, densely packed massive star cluster in our Galaxy that shows a high level of star formation activity. The nature of the extended non-thermal X-ray emission around the cluster remains unclear. The observed bright Fe $K\alpha$ line emission at 6.4 keV from material that is neutral or in a low ionization state can be produced either by X-ray photoionization or by cosmic-ray particle bombardment or both. In this paper we report on the first detection of the extended emission around the Arches cluster above 10 keV with the *NuSTAR* mission, and present results on its morphology and spectrum. The spatial distribution of the hard X-ray emission is found to be consistent with the broad region around the cluster where the 6.4 keV line is observed. The interpretation of the hard X-ray emission within the context of the X-ray reflection model puts a strong constraint on the luminosity of the possible illuminating hard X-ray source. The properties of the observed emission are also in broad agreement with the low-energy cosmic-ray proton excitation scenario.

Subject headings: Galaxy: center — ISM: general — cosmic rays — X-rays: individual (Arches cluster)

¹Space Science Lab, University of California, Berkeley, CA 94720; krivonos@ssl.berkeley.edu

²Instituto de Astrofísica, Facultad de Física, Pontificia Universidad Católica de Chile, 306, Santiago 22, Chile

³Space Science Institute, 4750 Walnut Street, Suite 205, Boulder, Colorado 80301

⁴MIT Kavli Institute for Astrophysics and Space Research, Cambridge, MA 02139, USA

⁵DTU Space - National Space Institute, Technical University of Denmark, Elektrovej 327, 2800 Lyngby, Denmark

⁶Lawrence Livermore National Laboratory, Livermore, CA 94550

⁷Cahill Center for Astronomy and Astrophysics, California Institute of Technology, Pasadena, CA 91125

⁸Columbia Astrophysics Laboratory, Columbia University, New York, NY 10027

⁹Harvard-Smithsonian Center for Astrophysics, 60 Garden Street, Cambridge, MA 02138, USA

¹⁰Jet Propulsion Laboratory, California Institute of Technology, Pasadena, CA 91109

¹¹NASA Goddard Space Flight Center, Greenbelt, MD

1. Introduction

The Arches cluster (G0.12+0.02, Cotera et al. 1996; Serabyn et al. 1998) is a massive star cluster with a core that is about $9''$ (~ 0.35 pc at 8 kpc) in radius (Figer et al. 1999), with an average mass density of $\sim 3 \times 10^5 M_{\odot} \text{pc}^{-3}$, containing more than 160 O-type stars (Figer et al. 2002). The Arches cluster is located in the inner Galactic Center (GC) region at the projected angular distance of $11'$ from the dynamic center of the Galaxy – Sagittarius A* (Sgr A*).

The first serendipitous *Chandra* observations of the Arches cluster region revealed two bright sources (A1 and A2) located in the cluster's core which are surrounded by the cluster's diffuse X-ray emission (Yusef-Zadeh et al. 2002). A1 was later resolved into two distinct bright sources: A1N and

A1S by Law & Yusef-Zadeh (2004) and Wang et al. (2006). Subsequent dedicated campaigns revealed a complicated picture of the Arches cluster X-ray emission, using spectral and morphological studies to establish the presence of thermal and non-thermal emission components. The thermal emission is thought to originate from multiple collisions between strong winds of massive stars (Chlebowski & Garmany 1991; Yusef-Zadeh et al. 2002; Wang et al. 2006; Capelli et al. 2011a). Diffuse non-thermal X-ray emission has been detected from a broad region around the cluster (Wang et al. 2006; Tsujimoto et al. 2007; Capelli et al. 2011b; Tatischeff et al. 2012). The non-thermal nature of this extended radiation is revealed by its bright fluorescent Fe K α 6.4 keV line emission. The Fe K α line at 6.4 keV, which is due to Fe that is neutral or in a low ionization state, is produced by ejecting a K-shell electron, either by hard X-ray photoionization from an external X-ray source, or by the collisional ionization induced by cosmic-ray (CR) accelerated electrons or ions (mainly protons and α -particles).

The mechanism producing the fluorescent line emission around the Arches cluster is not completely understood. The fluorescence may be the result of irradiation of the cloud by hard X-ray photons with energies above 7.1 keV (the K-edge of neutral iron). The required X-ray illumination might be associated with a nearby transient X-ray source (e.g. Churazov et al. 1993, for 1E1740.7-2942) or with past activity of Sgr A*, as suggested by Sunyaev et al. (1993) to explain the fluorescent line emission of the giant molecular cloud Sgr B2 in the GC region (Koyama et al. 1996; Sunyaev & Churazov 1998; Murakami et al. 2000; Revnivtsev et al. 2004a; Terrier et al. 2010). Alternatively, the excitation of cold material might be through the collisional ionization by CR particles (e.g. Predehl et al. 2003; Yusef-Zadeh et al. 2007; Dogiel et al. 2009). Tatischeff et al. (2012) (hereafter T12) argued that bright 6.4 keV line structures observed around the Arches cluster are very likely produced by bombardment of molecular gas by energetic ions, and they disfavored the possibility of accelerated electrons. T12 suggest that the required large flux of low-energy cosmic ray ions could be produced in the ongoing supersonic collision between the star cluster and a nearby molecular cloud.

Previously, the lack of spectral and morpholog-

ical studies above 10 keV precluded us from building a complete picture of the Arches cluster non-thermal emission and from making a definitive conclusion about the ionizing mechanism. With the first focused observations of the Arches cluster in the hard X-ray domain, we can shed light on the cause of the non-thermal X-ray emission detected around the cluster.

We assume a distance of 8 kpc to the GC (Gillessen et al. 2009) and the Arches cluster. Sect. 2 of the paper describes the *NuSTAR* observations and data reduction. In Sect. 3, we study the morphology of the Arches cluster using 2D image fitting procedures and wavelet image decomposition techniques. In Sect. 4, we present a spectral analysis using the background approach specially developed for *NuSTAR* observations. The main results are discussed in Sect. 5 and summarized in Sect. 6.

2. Observations and data reduction

We observed Arches cluster during the GC region campaign with the *Nuclear Spectroscopic Telescope Array (NuSTAR)* (Harrison et al. 2013) in October 2012. *NuSTAR* operates in wide energy band from 3 to 79 keV, carrying two identical co-aligned X-ray telescopes with an angular resolution of 18" (FWHM). The focal planes of each telescope, referred to as focal plane module A and B (FPMA and FPMB), provide a spectral resolution of 400 eV (FWHM) at 10 keV.

The first part of the survey was carried out in the inner GC region covering the area between Sgr A* and the persistent low-mass X-ray binary 1E 1743.1–2843 located 19' away (Porquet et al. 2003; Del Santo et al. 2006). The Arches cluster serendipitously appears in the three *NuSTAR* observations listed in Table 1.

We processed the data from both modules using the *NuSTAR Data Analysis Software (NuSTAR-DAS)* v1.2.0, the 2013 June 28 version of the *NuSTAR* Calibration Database (CALDB), and HEASOFT v6.13. The data were filtered for periods of Earth occultation, high instrumental background due to South Atlantic Anomaly (SAA) passages, and known bad/noisy detector pixels.

The *NuSTAR* detectors are not entirely shielded from X-rays that pass outside the X-ray optics modules and fall directly onto the detectors. Such

an unfocused flux or “stray-light” can be significant if there are bright X-ray sources within 2 – 3 degrees of the *NuSTAR* field of view (FOV). Stray-light from a point source has a uniform distribution on the detector and can be easily removed based on a geometrical model of the telescopes. We masked out the stray-light region of the FPMB detector (FPMA is clean) caused by two bright sources: GX 3+1 and the transient Swift J174510.8-262411 (see e.g. Vovk et al. 2012, and references herein), which was active at the time of the *NuSTAR* observations. The contaminated detector pixels have been flagged as “bad” and removed from the analysis at the stage of data screening in the *NuSTARDAS* pipeline run. The observation 40010003001 (FPMB) has been completely disregarded because stray-light completely covered the Arches cluster region.

Stray-light photons from the extended sources and known celestial X-ray backgrounds cannot be so easily removed because they fill the whole detector area and have a non-uniform pattern depending on the emission morphology. We treated this background differently for the imaging and spectral analysis. Regarding the former, the non-uniform background of the individual observations is effectively averaged when it is combined into the mosaic, and therefore, can be considered as nearly flat (however, see discussion in Sect. 3.1). In contrast, the non-uniformity of the background has a noticeable effect on the spectral analysis since it is done for individual observations. To overcome this issue we applied the approach described in Sect. 4.

After running the pipeline and screening the data, we end up with event lists for five *NuSTAR* observations containing the Arches cluster at different off-axis angles (Table 1). Note that the source appears at large off-axis distances, which causes the reduction of the efficiency (vignetting) and strong PSF distortion. The total nominal (effective) dead-time corrected exposure time of 122.5 (76.7) ks comprises 73.8 (44.7) ks and 48.7 (32.1) ks for FPMA and FPMB, respectively.

3. Morphology

The data from both detector modules were used to construct the mosaic images (Figure 1) around the Arches cluster in different energy bands. We used the 3 – 10 keV *NuSTAR* band as a proxy for

the standard 2 – 10 keV energy range; 6 – 7 keV band as containing Fe K α emission lines at 6.4 and 6.7 keV, which are unresolved by *NuSTAR*; and 10 – 20 keV as a hard X-ray band specific to *NuSTAR*. The mosaics in the energy bands 3 – 79, 20 – 40, and 40 – 79 keV are also shown in Figure 1. For each image an average (local) background level was determined within an annular region centered on the Arches cluster, as defined in Table 2 and illustrated in Figure 2. The background estimate was subsequently subtracted from each individual image, prior to the construction of the image mosaic. This is done because FPMB has a higher background count rate than FPMA, requiring that we adjust the relative detector background normalizations between modules. Note that the visible gradient in Figure 2 is produced mainly by the emission from the GC molecular clouds (see e.g. Ponti et al. 2010).

The exposure map, utilized for mosaic creation, has not been corrected for vignetting effects. We checked that the vignetting correction does not significantly improve the results of the imaging analysis. Hereafter, we assume no vignetting correction unless otherwise stated.

The primary goal of the current paper is to study the non-thermal emission surrounding the Arches cluster. The emission is revealed by fluorescent Fe K α 6.4 keV line, as has been observed by *XMM-Newton* and reported in the recent papers by Capelli et al. (2011a) and T12. We adopted T12 sky regions describing the core of the Arches cluster prominent in Fe K α 6.7 keV line (“Cluster” region) and the surrounding region characterized by the fluorescent 6.4 keV line (called “Cloud” region). The 6.7 keV line, attributed to the cluster core, originates from the hot, thermally-ionized plasma, probably from the colliding winds of the massive stars. The 6.4 keV line emission clearly extends beyond the Arches cluster core, and comes from material in neutral or low ionization states filling (in projection) an extended area represented by an ellipse as illustrated in Figure 1. The ellipse is oriented approximately in the North-South direction with increased brightness to the South. The parameters of the background and reference regions are listed in Table 2.

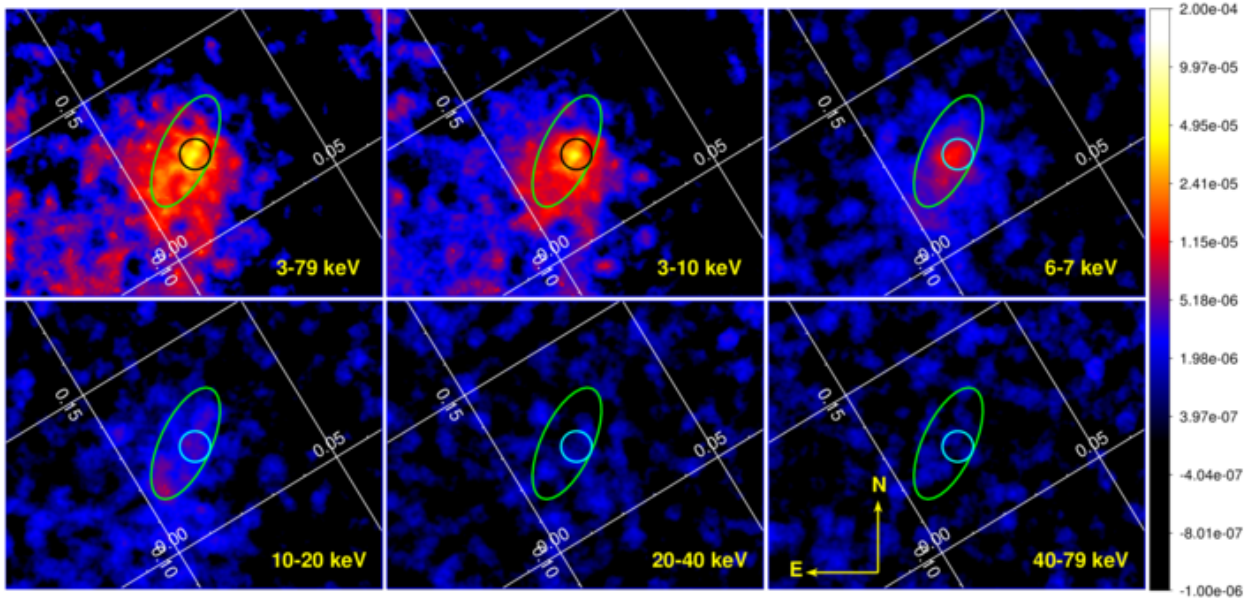


Fig. 1.— *NuSTAR* mosaic images of the Arches cluster in different energy bands. The images are background-subtracted, and adaptively smoothed with task *dmimgadapt* from CIAO-4.5 using a tophat kernel. The region used for local background estimation is shown in Figure 2. The cyan circle (in black on the two upper images) denotes the Arches cluster emission prominent at 6.7 keV (a He-like Fe $K\alpha$ line), and this region is denoted as “Cluster” in Table 2. The green ellipse represents the surrounding region characterized by the bright 6.4 keV line emission (“Cloud” region in Table 2). Both regions have been adopted from T12 for reference. The images are shown in the same log-scale color map shown on the right. The color bar is in units of $\text{cts s}^{-1}\text{pix}^{-1}$, and the angular size of the image pixel is $2''$. The white grid indicates Galactic coordinates in degrees. The compass sign shows the image alignment in equatorial coordinates, with North up and East to the left. The image orientation remains unchanged throughout the paper.

Table 1: Summary of the *NuSTAR* observations available for the Arches cluster.

Observation ID	Date 2012	Exposure ^a (ks)		Off-axis ^b (arcmin.)
		FPMA	FPMB	
40010003001	Oct 14	24.2 (17.0)	–	3.7
40010005001	Oct 15	26.0 (15.7)	25.6 (20.0)	4.1
40010006001	Oct 16	23.6 (12.0)	23.1 (12.1)	7.5

Notes. ^aContains dead-time corrected nominal exposure, whereas the effective exposure, estimated for vignetting at 8 keV, is listed in parentheses. ^bThe off-axis angle is calculated for the Arches cluster position with respect to the optical axis position on the detector.

3.1. Cluster emission

The Arches cluster has been relatively well studied in the standard 2 – 10 keV energy band with the *Chandra* and *XMM-Newton* observatories. Close attention has been paid to the central part of the cluster, where thermal emission, thought to be from colliding winds of giant stars, is observed. With data from *NuSTAR*, we can obtain new insight into the hard X-ray emission of the Arches cluster. However, even with angular resolution that is unprecedented for hard X-ray astronomy ($18''$ FWHM), it is challenging to resolve emission in the core, which has a radius of $\sim 15''$.

The 3 – 10 keV mosaic (Figure 1) demonstrates a strong excess in the core of the Arches cluster and apparent extended emission around it. To decouple these emission components and find the

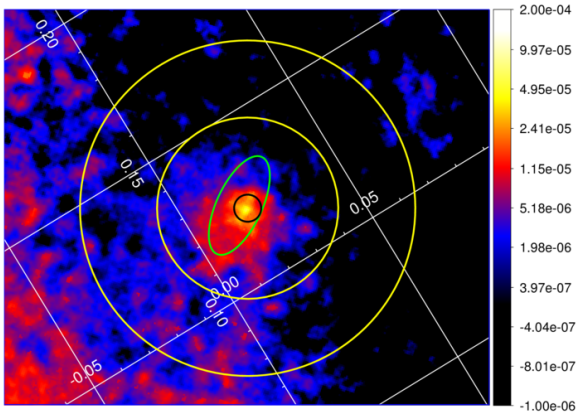


Fig. 2.— The definition of the local background region around the Arches cluster. The image shows the *NuSTAR* mosaic of the Arches cluster in the 3 – 10 keV energy band (see Figure 1 for the reference). The yellow annulus denotes the local background region used in the mosaic build up and fitting procedure (Sect. 3.1). The parameters of the annulus are listed in Table 2.

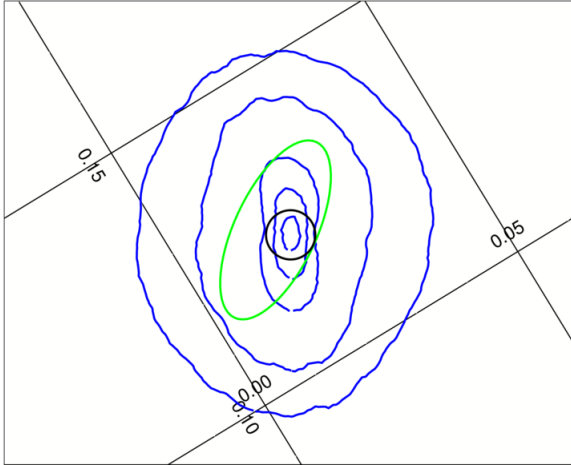


Fig. 3.— The average *NuSTAR* PSF in the 3 – 10 keV energy range. The blue contours denote PSF encircled energy levels for 10, 30, 50, 80, and 90%, respectively, going from the center outwards. The PSF was averaged over five observations listed in Table 1. The green ellipse and black circle represent Arches cluster emission regions, see Figure 1 for details.

centroid position of the core, we fitted a spatial model convolved with an averaged PSF on the combined data set using the *Sherpa* package (Freeman et al. 2001), which is part of the CIAO-4.5¹ software (Fruscione et al. 2006).

To make a PSF function representing the average over the different source offsets in the ObsIDs, we used the inflight-calibrated PSF shape stored in the CALDB. The PSF images were weighted according to the exposure time of each data set. The resulting averaged PSF is shown in Figure 3. Its shape is strongly distorted because of the large off-axis angles (on-axis PSF would be symmetric). Importantly, the PSF elongation is not co-aligned with the 6.4 keV line cloud region. For the fitting procedure, we assume no significant change of PSF shape inside the radius of 60'' around the Arches cluster (see below). Note that 90% of the averaged PSF encircled energy is situated at or inside of the inner radius of the annular region used for the background estimation, depending on the adopted energy used. Using this fact, we estimated the background count rate in the separate fitting procedure without PSF convolution.

Table 2: Definitions of the sky regions.

RA (J2000)	Dec (J2000)	Parameters
Cluster (circle)		
$17^h 45^m 50.3^s$	$-28^\circ 49' 19''$	15''
Cloud (ellipse)		
$17^h 45^m 51.0^s$	$-28^\circ 49' 16''$	25'', 59'', 155°
$17^h 45^m 50.3^s$	$-28^\circ 49' 19''$	15'' (excl.)
Background (annulus)		
$17^h 45^m 50.3^s$	$-28^\circ 49' 19''$	185''
$17^h 45^m 50.3^s$	$-28^\circ 49' 19''$	100'' (excl.)

Notes. Central position and radius for circular regions, and semi-minor/major axes and rotation angle for the elliptical regions. The rotation is defined counter clockwise relative to North (upward). “Cluster” and “Cloud” regions are illustrated in Figure 1. The excluded regions are marked as “excl.”.

Given the spatial extent of the emission around the Arches Cluster as found by Chandra and XMM-Newton, we want to confirm whether we can resolve this same emission with *NuSTAR*. This

¹<http://cxc.cfa.harvard.edu/ciao>

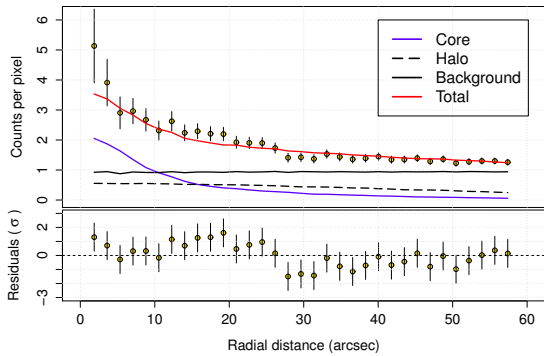


Fig. 4.— Radial profile of the Arches cluster region in the 3 – 10 keV energy band. Lines show the best-fit model and its components convolved with the averaged PSF.

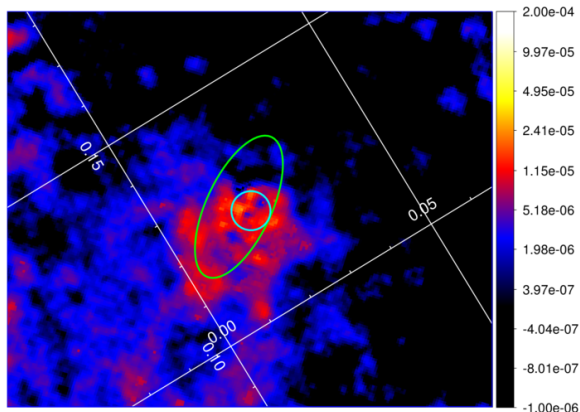


Fig. 5.— The *NuSTAR* 3 – 10 keV residual image of the Arches cluster after removal of the emission from the cluster’s core and background subtraction. The details of the region description can be found in Figure 1. The color bar units are $\text{cts s}^{-1}\text{pix}^{-1}$ and the angular pixel size is $2''$.

will give us confidence that we may also be able to spatially resolve the Arches cluster above 10 keV.

We represented the Arches cluster core emission by a 2D Gaussian. Due to the low count rate per pixel, we used Poisson statistics in the fitting procedure. The background term has been constrained in the annulus region shown in Figure 2. After running the fitting procedure with the 2D Gaussian model, we found that the 3 – 10 keV emission from the Arches cluster was not acceptably fitted with a single point source, and an extended “halo” around the cluster had to be considered. This finding is in line with the detection of extended emission surrounding the Arches cluster as observed by *Chandra* and *XMM-Newton* (Yusef-Zadeh et al. 2002; Law & Yusef-Zadeh 2004; Wang et al. 2006).

We constrained the fitting area to a circle centered on the core and extending to a radius of $60''$. The model includes (i) a narrow 2D Gaussian of fixed width ($4''$ FWHM, chosen to emulate the PSF smearing effect caused by incomplete aspect reconstruction), representing the cluster’s core, (ii) a wide 2D Gaussian describing the halo, and (iii) a constant background term. Note that the visible in Figure 2 background gradient has no significant effect on the fitting procedure. The best-fit model parameters are listed in Table 3. Figure 4 shows the radial profile of the Arches cluster intensity distribution centered at the best-fit position of the core.

To demonstrate a surface brightness distribution of the Arches cluster halo, we show in Figure 5 the residuals after subtracting off a best-fit point source corresponding to the core emission.

The position of the cluster’s core is spatially consistent with the brightest source, *A1*, detected by *Chandra* in the Arches cluster (Yusef-Zadeh et al. 2002) and later resolved into the two sources *A1S/N* (Law & Yusef-Zadeh 2004; Wang et al. 2006). Figure 6 shows confidence regions for the position uncertainty of the core and halo components.

Note that due to the *NuSTAR* optics design, the celestial coordinates of each incoming photon are determined during the post processing. This task is complicated by distortions due to thermal bending and external forces acting on the mast during orbit. The systematic offset of the

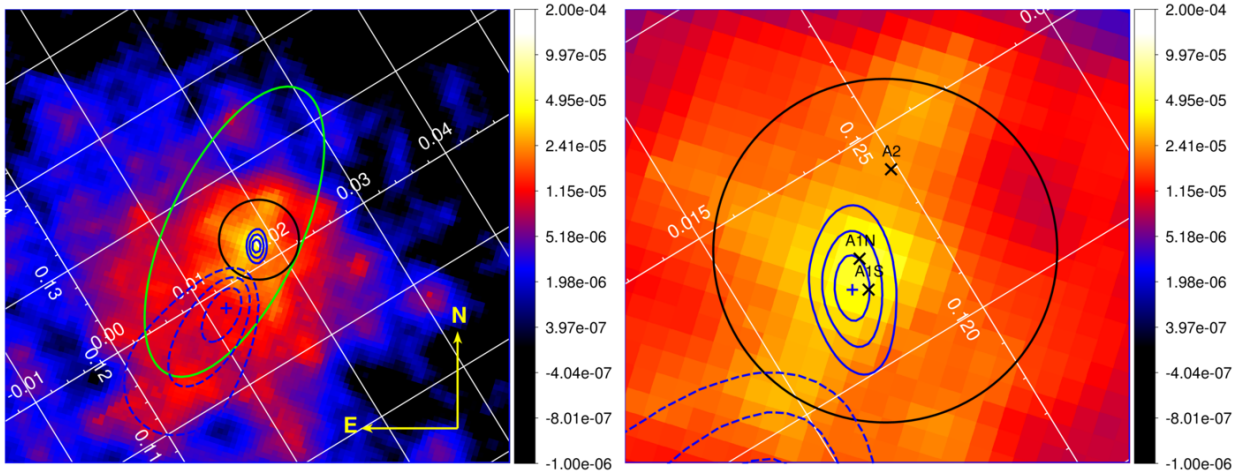


Fig. 6.— *Left*: Arches cluster core and halo centroid determination on the 3 – 10 keV *NuSTAR* mosaic image (use Figure 1 for the reference). Blue contours show 1-, 2- and 3- σ confidence intervals for the core (solid blue) and the halo (dashed blue) centroids. The centroid positions of the core and halo emission are marked as blue crosses. *Right*: A close-up of the region of the Arches core. Black points mark positions of three bright sources A1S/N and A2 that are resolved by *Chandra* observations of the Arches cluster (Wang et al. 2006). Note that a systematic scatter of $0.9''$ (RMS) is not taken into account (see Sect. 3.1). The color bar units are $\text{cts s}^{-1}\text{pix}^{-1}$ and the pixel size is $2''$.

source position determination can be as high as $10''$. However, the fact that the position of the Arches cluster core emission detected with *NuSTAR* is in agreement (within the angular separation of $\sim 1.5''$) with the catalogued coordinates of the two bright *Chandra* sources A1S/N, tells us that the described systematic offsets are negligible for these observations.

Our ability to centroid a weak source with *NuSTAR* is also subject to uncertainties based on how positions are probabilistically assigned to photons in the *NuSTARDAS* pipeline and the finite spatial resolution of the *NuSTAR* pixels. To estimate any scatter introduced by this process we ran the *NuSTARDAS* pipeline 50 times, repeated out analyses, and found that the sky position of the Gaussian core has an RMS scatter of $0.9''$. We adopt this as the systematic error on the cluster core position.

The width of the 2D Gaussian halo model component does not have strong physical meaning since this component is used specifically to describe local background of the core. However, we should note that the center position of the halo component does not coincide with the core centroid, and the trend suggests that the halo cen-

teroid falls outside the Arches cluster (Figure 6).

3.2. Wavelet decomposition

We studied in Sect. 3.1 the morphology of the Arches cluster in the 3 – 10 keV band fitting data with a parametric model. We constrained the central part of the cluster, determined its centroid position, flux, and revealed strong excess outside the cluster core. Since we observe extended emission with a complicated projected morphology, it becomes quite difficult to represent this emission with an analytical model, i.e. to parameterize it. In this case, *non-parametric* methods can be used for morphological studies. One such method is a wavelet image transform.

For the decomposition of *NuSTAR* images in different energy bands, we used the so called *à trous* digital wavelet transform algorithm (Starck & Murtagh 1994; Slezak et al. 1994; Vikhlinin et al. 1997; Krivonos et al. 2010). The main advantage of this algorithm over other wavelet methods is the fact that it decomposes the image into a linear combination of layers or “scales”, each of them emphasizes the structures with a characteristic size of $\approx 2^{J-1}$ pixels, which is 2^J arcseconds in

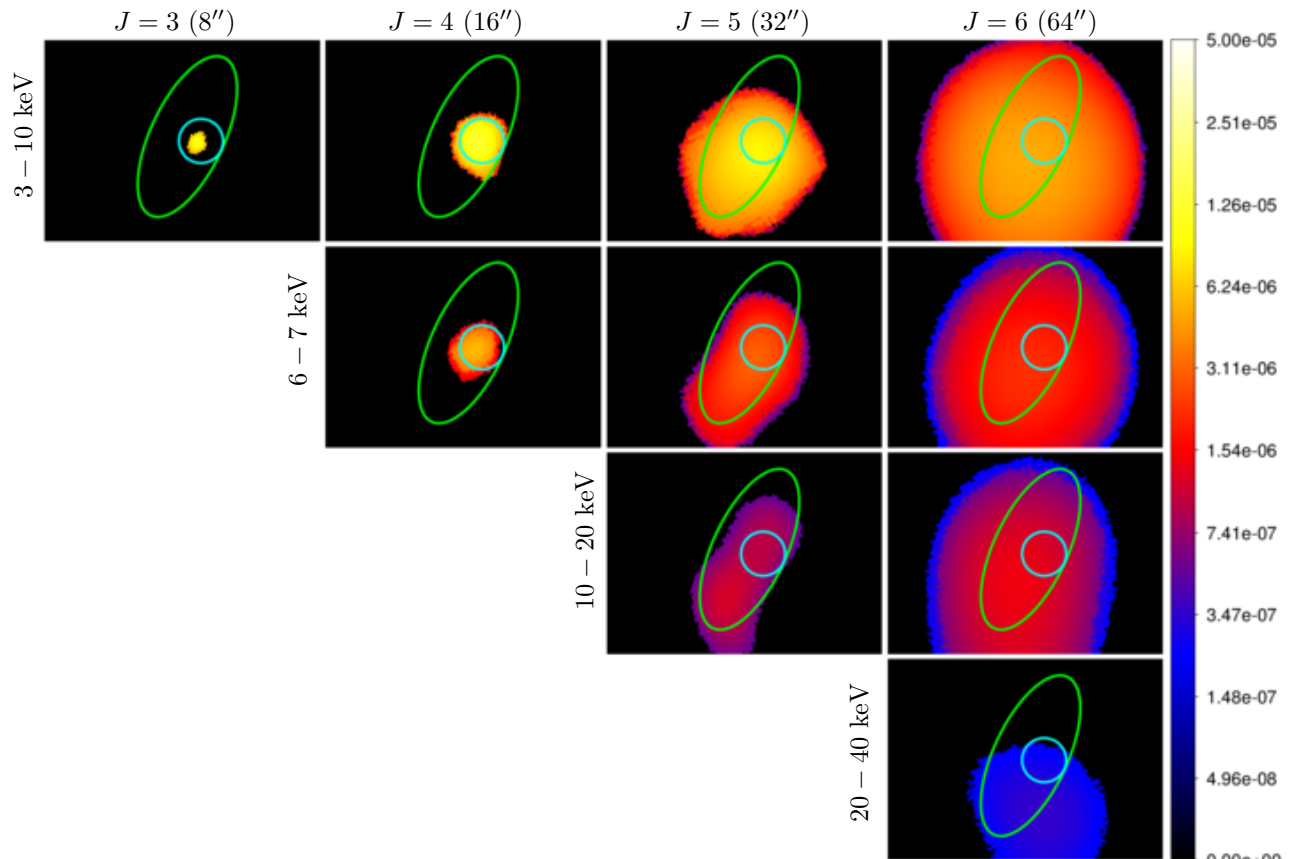


Fig. 7.— Wavelet decomposition of *NuSTAR* mosaic images of the Arches cluster in 3 – 10, 6 – 7, 10 – 20, and 20 – 40 keV energy bands. All structures with detection significance below 5σ have been removed from the images. The units of the color bar on the right are $\text{cts s}^{-1}\text{pix}^{-1}$, where the pixel size is $2''$.

the case of our *NuSTAR* mosaic image resolution ($1\text{pix} = 2''$). Thus, low (high) J values correspond to small (large) spatial variations. We used the *WVDECOMP* wavelet decomposition code developed by Vikhlinin et al. (1995, 1998) as a part of *ZHTOOLS* software package².

We ran *WVDECOMP* on mosaic images for scales 1 – 7 ($2'' - 128''$), detecting all significant structures above the 5σ level. To keep the photon statistics on the images, we provided counts and exposure maps to *WVDECOMP*. As mentioned in Sect. 3, FPMB has a higher background count rate than FPMA. In fact, this can mimic extended structures on the exposure-corrected image. To diminish this effect, we built the background map

for a given observation by multiplying the exposure map and background count rate measured in the annulus region shown in Figure 2. The individual background maps were combined into the mosaic and used as a part of the *WVDECOMP* algorithm.

Figure 7 shows wavelet scales 3 – 6 of the Arches cluster mosaic images in 3 – 10, 6 – 7, and 10 – 20 keV. The lowest scales (1, 2) do not contain significantly detected (5σ) structures. The highest scale (7) contains large-scale diffuse background attributed to the Galactic center molecular complex zone (Ponti et al. 2010) and Galactic Ridge X-ray Emission (GRXE, see e.g. Revnivtsev et al. 2006). We combined scales 3 – 6, which only contain structures related to the Arches cluster into the mosaics shown in Figure 8. The main results

²<http://hea-www.harvard.edu/RD/zhtools>

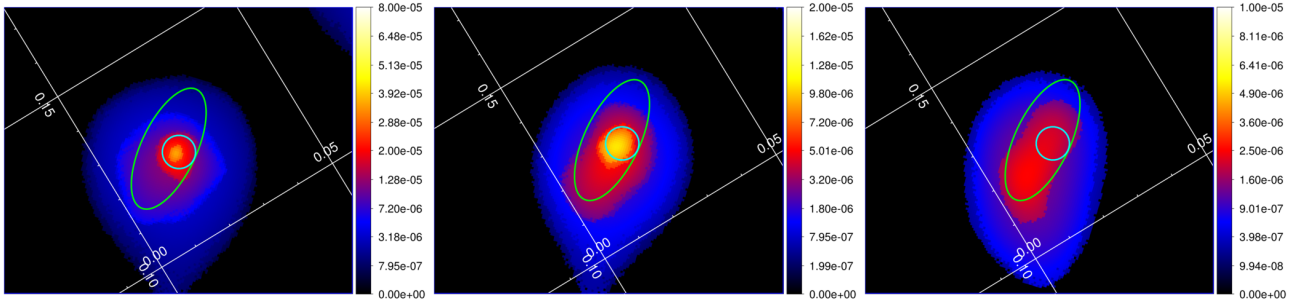


Fig. 8.— Stacked wavelet layers (see Figure 7) of the Arches cluster *NuSTAR* mosaic images in the (from left to right) 3 – 10, 6 – 7, and 10 – 20 keV energy bands. All structures with detection significance below 5σ have been removed from the images. The units of the images are $\text{cts s}^{-1}\text{pix}^{-1}$ and the pixel size is $2''$.

Table 3: Best-fit model parameters for the PSF fitting procedure of the 3 – 10 keV Arches cluster core and halo emissions.

Parameter	Value
Background (constant)	
Norm. ($\times 10^{-5}$)	$1.18 \pm 0.01 \text{ cnts s}^{-1} \text{ pix}^{-1}$
Core (2D Gaussian)	
Center R.A. ^a	$17^{\text{h}}50^{\text{m}}50.43^{\text{s}}$
Center Dec. ^a	$-28^{\circ}49'23.07''$
FWHM	$4.0''$ (fixed)
Norm. ($\times 10^{-3}$)	$2.2 \pm 0.3 \text{ cnts s}^{-1} \text{ pix}^{-1}$
Halo (2D Gaussian)	
Center R.A. ^a	$17^{\text{h}}45^{\text{m}}50.62^{\text{s}}$
Center Dec. ^a	$-28^{\circ}49'47.17''$
FWHM	$72'' .4^{+6''.7}_{-4''.7}$
Norm. ($\times 10^{-5}$)	$1.77^{+0.45}_{-0.37} \text{ cnts s}^{-1} \text{ pix}^{-1}$
Cash statistic	4661.91
Degrees of freedom	2820

Notes. ^aJ2000 epoch, the 1σ positional uncertainty is less than $2''$ and $6 - 8''$ for the core and halo components, respectively, see 2D confidence regions in Figure 6 for details. Model normalization factor is marked as “Norm.”.

from the WT decomposition can be summarized as follows (refer to Figs. 7 and 8).

3 – 10 keV: The core of the Arches cluster is clearly visible on the scales $J = 3 - 4$ and the halo emission is revealed on scale $J = 5$. The apparent position of the halo is consistent with fitting results in Sect. 3.1 showing a shifted position with respect to the cluster core.

6 – 7 keV: This energy band contains two blended Fe $K\alpha$ lines at 6.4 and 6.7 keV. We speculate that these lines appear at scales $J = 4$ (6.7 keV) and $J = 5$ (6.4 keV). The 6.7 keV line is spatially consistent with core emission, while the 6.4 keV line emission follows the cloud region as expected. These results are in full agreement with *XMM-Newton* observations (T12). In contrast to the 3 – 10 keV band, the 6.7 keV line emission distribution does not demonstrate high-frequency detection at $J = 3$, which may indicate its broader spatial distribution in comparison with the 3 – 10 keV continuum emission of the Arches cluster. However we should note that the 6 – 7 keV mosaic image is not continuum subtracted.

10 – 20 keV: The Arches cluster does not show any significant ($> 5\sigma$) point-like structures in the core region, which is expected due to the rapid fall of the ~ 1.7 keV thermal emission above 10 keV. On the other hand, the hard X-ray emission is significantly detected at scales $J = 5 - 6$. Note that the observed extended structure cannot be caused by the wide wings of the PSF – as is demonstrated in Figure 3, the PSF shape is not aligned with the cloud region morphology. The observed 10 – 20 keV continuum emission apparently coincides with Fe $K\alpha$ fluorescent 6.4 keV line emission

observed with *XMM-Newton* (T12). According to T12, the 6.4 keV line emission demonstrates brightening in the south-east part of the ellipse, which is also noticeable at scale $J = 5$.

20 – 40 keV: The mosaic map of the Arches cluster shown in Figure 1 does not allow to make a definitive conclusion about the source detection. However, wavelet decomposition shows weak excess at scale $J = 6$. This fact is implicitly confirmed by detection of the emission up to 40 keV in the spectral analysis of Sect. 4. The apparent hard X-ray emission is located outside the cluster and consistent with general extent of 10 – 20 keV emission.

4. Spectroscopy

We extracted spectral information for the Arches cluster from the circular region with radius of $50''$ centered at the cluster’s core (Table 2), including the core and extended emission. The spectra have been extracted from all observations using the *nuproducts* task applying PSF and ghost ray corrections to the effective area ARF (Ancillary Response File).

The extraction of the corresponding background spectra is complicated by the strong CXB and GRXE stray-light illumination causing a non-uniform pattern on the detectors with a gradient of a factor of two. For that reason, the background spectrum extracted from the source-free region over- or underpredicts the background count rate at the position of the source. This difficulty (not relevant for spectra of bright sources) causes strong systematic noise for the background-subtracted spectrum of weak sources such as Arches. To overcome this, we use the fact that the stray-light background does not significantly change for sky pointings separated by only $10\text{--}20'$, and therefore we utilize nearby observations. Note that this method differs from that used in the imaging analysis. In the paired observation, we extract the background spectrum from the same detector region where the Arches cluster was observed. Obviously, this region should not contain any other diffuse or point-like source or stray-light from nearby bright sources. Table 4 lists the observations used for source and background spectrum extraction. For *ObsID* 40010006001, we had three observations which were suitable for background

spectrum extractions and thus averaged together for better statistics.

Using the above-mentioned method, we have constructed one FPMB and three FPMA spectra. The latter have been further grouped together using the FTOOL task MATHPHA. The corresponding background spectra and responses have been averaged accordingly. Finally we have grouped spectrum channels to have at least 30 counts per bin using GRPPHA tool. Figure 9 shows the FPMA and FPMB spectra of the Arches cluster.

According to the morphological studies presented in Sect. 3, we attribute the hard spectral component above 10 keV to the fluorescing cloud around the Arches cluster.

We first approximated the observed spectra with the collisionally ionized plasma emission model APEC representing the cluster’s core thermal emission, and a non-thermal power-law continuum with a Gaussian line at 6.4 keV, modeling the cloud emission outside the cluster (Figure 9). Due to the fact that *NuSTAR* has a limited spectral resolution, the centroid energy of the Gaussian line and its width have been fixed at 6.4 keV and 0.1 keV, respectively. All the emission components were subject to a line-of-sight photoelectric absorption model WABS in XSPEC. The fitting procedure does not allow us to constrain the absorption, and we fixed it at $N_{\text{H}} = 9.5 \times 10^{22} \text{ cm}^{-2}$ measured by T12 (also using WABS) in the core of the Arches cluster. The metallicity of the X-ray emitting plasma was not constrained either, and we fixed it to $Z = 1.7Z_{\odot}$ as per T12. The best-fit results obtained with this model (referred as model 1 in the discussion) are shown in Table 5. All fitted parameters in this table and in the following discussion contain uncertainty estimation at the 90% confidence level.

Model 1 provides a reliable fit to the data by constraining the temperature of the core emission, the power-law component and the intensity of the 6.4 keV line. The $1.76_{-0.29}^{+0.36}$ keV temperature of the thermal component is in agreement with that recently measured by T12 in the cluster’s core ($1.79_{-0.05}^{+0.06}$ keV from “model 1” in T12). The power-law slope $\Gamma = 1.62 \pm 0.31$ is consistent with $\Gamma = 1.6_{-0.2}^{+0.3}$ from T12, measured in the cloud region. T12 finds the slope and 6.4 keV line equivalent width ($EW_{6.4 \text{ keV}}$) of the cloud region compatible with the low-energy cosmic-ray

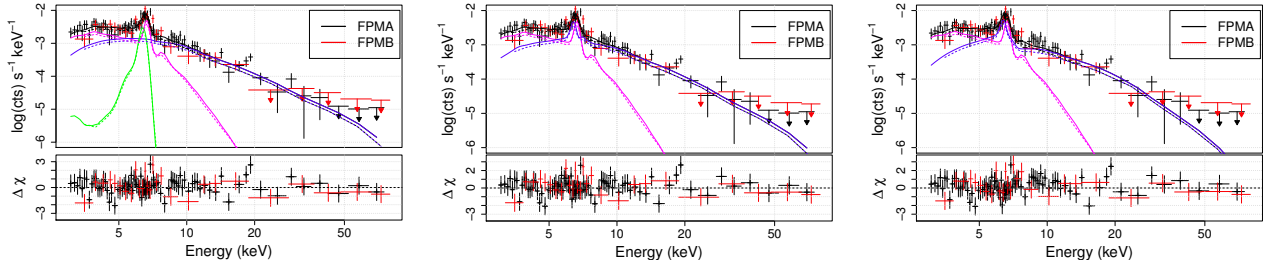


Fig. 9.— The X-ray spectrum of the Arches cluster as measured with *NuSTAR* FPMA (black) and FPMB (red). The spectra are fitted with models all containing APEC component (magenta) and: model 1 (left) – power-law (blue) and Gaussian (green); model 2 (middle) – *LECRp* (blue); model 3 (right) – *REFLIONX* (blue); see Table 5 for details. Solid lines represent model components for FPMA, and dotted for FPMB, respectively.

Table 4: Observations used for source and background spectral extraction.

Source spectrum (ObsID ^a)	Background spectrum (ObsID ^a)
40010003001A ^b	40010001001A
40010005001A	40010003001A ^b
40010006001A/B ^c	40010001002A/B
	40010003001A/B
	40010005001A/B

Notes. ^a The name of the focal plane module (A or B) is attached to the end of the ObsID. ^b The corresponding FPMB data has strong stray-light contamination, see Sect. 2. ^c The background spectrum has been averaged over three observations.

(LECR) ion model, where collisional ionization of the cloud by cosmic ray (CR) protons produces the 6.4 keV fluorescence line. According to the *XMM-Newton* study of the Arches cluster by T12, the *LECR electron* model (*LECR_e*) requires an ambient Fe abundance $\gtrsim 3$ times the solar value to account for the measured *EW* of 1.2 ± 0.2 keV, which makes the measured properties of the non-thermal cloud region emission hardly compatible with the *LECR electron* model. We consider only the *LECR proton* (*LECR_p*) model in the following analysis.

We fitted the spectra with the XSPEC model $WABS \times (APEC + LECRp)$, henceforth “model 2”. The model depends on the *LECR* path length in the ambient medium, Λ , the minimum energy

of the CR particles entering the cloud, E_{min} , the power-law index of the CR source energy spectrum, s , and the metallicity of the X-ray emission region, Z . We fixed Λ and E_{min} parameters of the *LECR_p* model according to T12, making free slope s and normalization N_{LECR} . The best-fit results obtained with model 2 are given in Table 5 and the spectral components are shown in Figure 9.

The *NuSTAR*-measured spectral index of the injected low-energy protons $s = 1.65^{+0.59}_{-0.55}$ is in general agreement with the T12 value ($1.9^{+0.5}_{-0.6}$). The best-fit *LECR* model normalization for the fixed $E_{min} = 10$ MeV nucleon⁻¹ $N_{LECR} = (8.08^{+1.82}_{-1.62}) \times 10^{-8}$ erg cm⁻² s⁻¹ is somewhat higher than that measured by T12 ($N_{LECR} = (5.6^{+0.7}_{-0.3}) \times 10^{-8}$ erg cm⁻² s⁻¹). The corresponding power injected by *LECR* protons lies in the range $(5 - 8) \times 10^{38}$ erg s⁻¹.

To test the X-ray reflection scenario of the Arches cluster non-thermal emission, we applied the self-consistent reflection model *REFLIONX*³ in XSPEC describing the reflected spectrum for an optically thick atmosphere of constant density, illuminated by radiation with a power-law spectrum (Ross & Fabian 2005), henceforth “model 3”. The *REFLIONX* spectrum contains modeled fluorescence lines and continuum emission (Figure 9). Developed for the surface of hot accretion disks, *REFLIONX* can still be applied for cold material around the Arches cluster, fixing the ionization parameter ξ at the lowest allowed value of 10 erg cm s⁻¹. The best-fit parameters of model 3

³<http://heasarc.gsfc.nasa.gov/xanadu/xspec/models/reflion.html>

Table 5: Spectral analysis of the Arches cluster X-ray emission.

Parameter	(Unit)	Model 1	Model 2	Model 3
C		1.06 ± 0.14	1.05 ± 0.14	1.07 ± 0.14
N_H	(10^{22}cm^{-2})	9.5 (fixed)	9.5 (fixed)	9.5 (fixed)
Z/Z_\odot		1.7 (fixed)	1.7 (fixed)	1.7 (fixed)
kT	(keV)	$1.76^{+0.36}_{-0.29}$	$1.69^{+0.31}_{-0.26}$	$1.64^{+0.37}_{-0.23}$
I_{kT}	(see notes)	$36.0^{+17.8}_{-12.9}$	$39.6^{+16.7}_{-11.9}$	$43.2^{+16.9}_{-15.0}$
$E_{6.4 \text{ keV}}$	(keV)	6.4 (fixed)	–	–
$F_{6.4 \text{ keV}}$	$(10^{-5} \text{ph cm}^{-2} \text{s}^{-1})$	1.24 ± 0.5	–	–
Γ		1.62 ± 0.31	–	–
$I_{\text{p.l.}}$	$(10^{-12} \text{erg cm}^{-2} \text{s}^{-1} \text{ over } 3\text{-}20 \text{ keV})$	$1.49^{+0.26}_{-0.24}$	–	–
$EW_{6.4 \text{ keV}}$	(keV)	$1.1^{+0.7}_{-0.5}$	–	–
Λ	(H-atoms cm^{-2})	–	5×10^{24} (fixed)	–
s		–	$1.65^{+0.59}_{-0.55}$	–
E_{min}	(keV/n)	–	10^4 (fixed)	–
N_{LECR}	$(10^{-8} \text{ erg cm}^{-2} \text{ s}^{-1})$	–	$8.08^{+1.82}_{-1.62}$	–
Γ_{RX}		–	–	2.93 ± 0.31
ξ	erg cm s^{-1}	–	–	10 (fixed)
I_{RX}	(10^{-5})	–	–	6.09 ± 5.00
Reduced χ^2 (d.o.f.)		0.91 (134)	0.89 (136)	0.91 (140)

Notes. Model 1: $C \times \text{WABS} \times (\text{APEC} + \text{Gaussian} + \text{powerlaw})$; Model 2: $C \times \text{WABS} \times (\text{APEC} + \text{LECR}p)$; Model 3: $C \times \text{WABS} \times (\text{APEC} + \text{REFLIONX})$. The cross-calibration constant term C is fixed at unity for FPMA data and fitted for FPMB. The absorption column density is noted as N_H . APEC thermal plasma model is characterized by kT , Z/Z_\odot , and I_{kT} parameters, respectively, describing temperature, metallicity relative to solar, and normalization in units of $10^{-18} \int n_e n_H dV / (4\pi D^2)$, where n_e and n_H are the electron and proton number densities in units of cm^{-3} , and D is the distance in cm. $E_{6.4 \text{ keV}}$ and $F_{6.4 \text{ keV}}$: centroid energy and flux of the neutral or low-ionization Fe $K\alpha$ line. Γ and $I_{\text{p.l.}}$: index and 3 – 20 keV pegged normalization of the power-law component (model PEGPWRLW). $EW_{6.4 \text{ keV}}$: EW of the 6.4 keV line with respect to the power-law continuum. Λ , s , E_{min} , and N_{LECR} : LECR ions path length, source spectrum index, minimum energy, and model normalization. By definition $dW/dt = 4\pi D^2 N_{\text{LECR}}$ is the power injected in the interaction region by primary CR protons with energies between E_{min} and $E_{\text{max}} = 1 \text{ GeV}$, where D is the distance to the source. Γ_{RX} , ξ , and I_{RX} : the power-law slope of the incident radiation, ionization parameter (defined as $\xi = 4\pi F_{\text{tot}}/n_H$ where F_{tot} is the total illuminating flux, and n_H is the density of the reflector), and normalization of REFLIONX model (Ross & Fabian 2005). The metallicity parameter Z for LECR and REFLIONX models is fixed at $1.7Z_\odot$. Reduced χ^2 (d.o.f.): reduced χ^2 and degrees of freedom.

are shown in Table 5.

5. Discussion

In this section we discuss the results of this work in the context of two scenarios proposed to explain the excitation mechanism of the fluorescent emission around the Arches cluster.

5.1. CR bombardment hypothesis

A particle bombardment excitation scenario for the Fe fluorescence line emission involves the interaction of CR ions with cold molecular gas. T12 developed a steady-state slab model in which accelerated particles penetrate a cloud of neutral gas at a constant rate until they either stop or escape from the cloud. The model describes the properties of the neutral Fe $K\alpha$ line emission excited by impacts of LECR ions. These authors argue that fluorescent 6.4 keV line emission of the Arches cluster is excited by LECR protons with a relatively soft incident spectrum $s = 1.9^{+0.5}_{-0.6}$. Our *NuSTAR* spectral analysis (model 2) implies a somewhat harder slope $s = 1.65^{+0.59}_{-0.55}$, however, both measurements are consistent within the error intervals. T12 notes that production of 6.4 keV line photons by LECR collisional ionization is relatively inefficient and that high power in LECRs is needed to produce the observed fluorescent Fe $K\alpha$ line flux. As the authors suggest, a large flux of LECR ions could be produced in the ongoing supersonic collision between the star cluster and nearby molecular cloud.

Note that LECR p model provides an equally good fit as the reflection model discussed below.

5.2. X-ray reflection hypothesis

By definition, the excitation of the neutral material of the cloud by hard X-ray irradiation implies a transient or persistent X-ray source outside or within the cloud.

Assuming that the irradiation source is located in the Arches cluster, the source luminosity required to produce the observed 6.4 keV line flux can be estimated from the fluorescent model described in Sunyaev & Churazov (1998). Applying this approach on the *XMM-Newton* data, T12 showed that the luminosity of the source in the cluster must be at least 10^{36} erg s^{-1} . However,

the persistent X-ray luminosity is far below this level. Capelli et al. (2011a) recently reported X-ray flaring activity in the core of the Arches cluster, probably originating from stellar wind interactions in one or more massive binary systems. Such transient activity, in principle, can trigger fluorescent emission of the neutral material outside the Arches cluster, but the peak luminosity of the observed flare is far below the threshold mentioned above.

The illuminating source could also be a transient X-ray binary system. Their typical X-ray luminosity can reach levels on the order of $10^{36} - 10^{38}$ erg s^{-1} for high- and low-mass systems. If the bright state of an X-ray binary lasted for more than 8 years at or above 10^{37} erg s^{-1} , it would be sufficient for the observed 6.4 keV flux (Capelli et al. 2011b). However, such a long outburst is much longer than typical flaring timescales of X-ray transients (Degenaar & Wijnands 2010), though, at least one exceptional case is known, the neutron star X-ray transient KS 1731-260 (Sunyaev & Kwant Team 1989; Sunyaev et al. 1990) which became quiescent after more than a decade in the bright state (Wijnands et al. 2001; Revnivtsev & Sunyaev 2002).

The *NuSTAR*-measured EW of the 6.4 keV line with respect to the power-law continuum, $EW_{6.4 \text{ keV}} = 1.1^{+0.7}_{-0.5}$ keV, is in agreement with previous studies performed on spatially resolved fluorescent clouds around the Arches cluster (Capelli et al. 2011b, T12). In the context of an X-ray reflection scenario, the relatively high EW of the Fe $K\alpha$ line indicates a scattered emission component (assuming normal Fe abundance) or strong photoabsorption (Sunyaev & Churazov 1998), which can explain the fact that the direct source of photoionization is not seen by the observer. However, according to *NuSTAR* maps of the Arches cluster above 10 keV (Figure 1), for which the efficiency of photoabsorption rapidly falls, no significant source has been detected.

The Arches cluster spectrum is well-fitted with a model composed of an optically thin thermal plasma and an X-ray reflection component (Figure 9). The spectrum of the illuminating X-ray source is estimated to have relatively soft slope $\Gamma_{\text{RX}} = 2.93 \pm 0.31$. We may assess the luminosity of the primary source L_{RX} required by the reflection component following the method used by Reis

et al. (2013) to estimate the reflection fraction R . This parameter is defined as a measure of the ratio of the reflected flux to the continuum power-law flux. REFLIONX calculates R by dividing the extrapolated (1 eV – 1000 keV) REFLIONX flux by the 100 eV – 1000 keV power-law flux. On the other hand, the reflection scaling factor R is in fact the solid angle $R = \Omega/2\pi$ subtended by the reflecting cloud ($R = 0$ means no reflection). We estimated the unabsorbed 0.3 – 8 keV luminosity L_{RX} (at 8 kpc) for the tabulated R values – 0.5, 1.0 (source above a plane), 1.5 and 2.0 (source inside the cloud) as 2.5, 1.3, 0.8 and 0.6×10^{36} erg s $^{-1}$, respectively. Wang et al. (2006) reported the 0.3 – 8 keV luminosity of the bright Arches cluster sources A1N/S and A2, respectively, as 7.2 (A1N), 11 (A1S), and 4.6×10^{33} erg s $^{-1}$, which is 1 – 2 orders of magnitude below the luminosity of the illuminating continuum required by the reflected component. This constraint is consistent with what can be drawn from the observed 6.4 keV line flux, using the general idea of Sunyaev & Churazov (1998), as demonstrated by T12.

The interpretation of the observed spectra with the X-ray reflection model confirms that the Arches cluster itself is unlikely to be the source of the cloud fluorescence emission.

The non-detection of Fe K α line flux variability over more than eight years of *XMM-Newton* observations (Capelli et al. 2011b, T12) puts strong limits on the photoionization excitation of molecular clouds around the Arches cluster by a hard X-ray source. Nevertheless, the plausibility of the scenario with an earlier outburst of Sgr A* is under debate. The large scale spatial distribution and time variation of the Fe-K fluorescence seen in the GC region reveal the apparent superluminal propagation of a light front illuminating a molecular nebula (Ponti et al. 2010). In this context, it is quite reasonable to anticipate X-ray photoionization of the molecular clouds near the Arches cluster by Sgr A*. A possible decrease in the 6.4 keV flux with time would be expected in this scenario. For instance, strong variability of the 6.4 keV emission has been detected in Sgr B2 (Terrier et al. 2010) after ten years of a persistent state as shown by Revnivtsev et al. (2004a) – however see Inui et al. (2009). Capelli et al. (2011b) found the relatively constant 6.4 keV flux of the Arches cluster clouds consistent with a long

outburst from Sgr A* at a constant luminosity of 1.4×10^{39} erg s $^{-1}$ (Ponti et al. 2010). On the other hand, Clavel et al. (2013) possibly revealed a highly variable active phase of Sgr A* during the past few hundred years.

The measured power-law slope of the illuminating source in the model 3 (Sect. 4) is softer ($\Gamma \approx 3$) than observed for Sgr A* flares (Porquet et al. 2003, 2008; Nowak et al. 2012, Barriere et al. 2013, submitted to ApJ). Additionally, the slope is softer than that estimated by Revnivtsev et al. (2004b) for Sgr B2 in the context of Sgr A* reflected emission. However, we should note that REFLIONX calculates the reflected spectrum for an optically thick atmosphere while the molecular clouds close to the Arches cluster exhibit transparency at $\tau < 1$ (Capelli et al. 2011b). A more realistic reflection model at lower τ values and different source-cloud geometry settings can produce a harder spectrum of the primary emission.

6. Summary

In this paper we present results on the first focused hard X-ray observation of the Arches cluster performed by *NuSTAR*. We report on significant detection of the hard X-ray emission around the cluster with a spectrum that extends for the first time up to ~ 40 keV. The main results can be summarized as follows:

- The *NuSTAR* mosaic image of the Arches cluster shows a core component and extended halo emission in the 3–10 keV energy band. The centroid position of the core emission coincides with the bright sources A1N/S resolved with *Chandra* in the Arches cluster. The halo emission around the cluster also follows the morphology observed with *Chandra*. The centroid position of the halo emission does not coincide with the core and tends to be outside the Arches cluster.
- Wavelet decomposition of sky mosaics does not show any significant (5σ) detection of point-like sources in the core of the Arches cluster above 10 keV. The continuum 10 – 20 keV emission is significantly detected well beyond the Arches cluster with a spatial morphology consistent with the Fe K α fluorescent 6.4 keV line emission observed with

XMM-Newton (T12).

- The spectral analysis of the Arches cluster region, including the extended emission around it, reveals a ~ 1.7 keV temperature plasma, which is consistent with the optically thin thermal plasma measured by T12 in the cluster's core and associated with thermalization of massive star winds and several colliding stellar wind binaries within the cluster (T12).
- The power-law slope $\Gamma = 1.62 \pm 0.31$ and $EW_{6.4 \text{ keV}} = 1.1^{+0.7}_{-0.5}$ keV are in agreement with that measured by T12 around the Arches cluster and expected for the LECR ion model.
- The X-ray emission of the Arches cluster is well fitted with a model composed of an optically thin thermal plasma and a non-thermal component produced by LECR ions (T12). The best-fit CR spectral index is $s = 1.65^{+0.59}_{-0.55}$. The LECR model normalization gives the corresponding power of the injected LECR protons in the cloud region at the level of $(5 - 8) \times 10^{38} \text{ erg s}^{-1}$ (with $D=8$ kpc and CR minimum energy $E_{\text{min}} = 10 \text{ MeV nucleon}^{-1}$).
- The luminosity of the primary source required by the X-ray reflection model is 1 – 2 orders of magnitude higher than that observed in the Arches cluster, which is in agreement with similar constraints drawn from the 6.4 keV line flux.

The X-ray photoionization and CR-induced emission models can reproduce the data equally well. Additional *NuSTAR* observations with the Arches cluster on-axis would be useful to detect the difference between the emission models above 20 keV. At this point, we can conclude that explaining the non-thermal emission around the Arches cluster with an X-ray reflection scenario in which the illuminating source is located in or close to the cluster is unlikely. However irradiation by a long outburst of Sgr A* can still be considered, and would imply long-term variability of the 6.4 keV line flux should be detected. The excitation of the neutral material around the cluster by CR interactions also looks plausible, though

a large flux of LECR protons is needed to produce the observed fluorescent emission.

This work was supported under NASA Contract No. NNG08FD60C, and made use of data from the *NuSTAR* mission, a project led by the California Institute of Technology, managed by the Jet Propulsion Laboratory, and funded by the National Aeronautics and Space Administration. We thank the *NuSTAR* Operations, Software and Calibration teams for support with the execution and analysis of these observations. This research has made use of the *NuSTAR* Data Analysis Software (*NuSTARDAS*) jointly developed by the ASI Science Data Center (ASDC, Italy) and the California Institute of Technology (USA). FEB acknowledges support from Basal-CATA (PFB-06/2007) and CONICYT-Chile (FONDECYT 1101024 and Anillo ACT1101). RK thanks Eugene Churazov for fruitful discussions and valuable suggestions to the paper.

Facilities: NuSTAR.

REFERENCES

- Biviano, A., Durret, F., Gerbal, D., Le Fevre, O., Lobo, C., Mazure, A., & Slezak, E. 1996, *A&A*, 311, 95
- Bélanger, G., Goldwurm, A., Goldoni, P., et al. 2004, *ApJ*, 601, L163
- Capelli, R., Warwick, R. S., Cappelluti, N., et al. 2011a, *A&A*, 525, L2
- Capelli, R., Warwick, R. S., Porquet, D., Gillessen, S., & Predehl, P. 2011b, *A&A*, 530, A38
- Chlebowski, T., & Garmany, C. D. 1991, *ApJ*, 368, 241
- Churazov, E., Gilfanov, M., Sunyaev, R., et al. 1993, *ApJ*, 407, 752
- Clavel, M., Terrier, R., Goldwurm, A., et al. 2013, arXiv:1307.3954
- Cotera, A. S., Erickson, E. F., Colgan, S. W. J., et al. 1996, *ApJ*, 461, 750
- Degenaar, N., & Wijnands, R. 2010, *A&A*, 524, A69

- Del Santo, M., Sidoli, L., Bazzano, A., et al. 2006, *A&A*, 456, 1105
- Dogiel, V., Cheng, K.-S., Chernyshov, D., et al. 2009, *PASJ*, 61, 901
- Figer, D. F., Kim, S. S., Morris, M., et al. 1999, *ApJ*, 525, 750
- Figer, D. F., Najarro, F., Gilmore, D., et al. 2002, *ApJ*, 581, 258
- Freeman, P., Doe, S., & Siemiginowska, A. 2001, *Proc. SPIE*, 4477, 76
- Fruscione, A., McDowell, J. C., Allen, G. E., et al. 2006, *Proc. SPIE*, 6270,
- Gillessen, S., Eisenhauer, F., Trippe, S., et al. 2009, *ApJ*, 692, 1075
- Grebenev, S. A., Forman, W., Jones, C., & Murray, S. 1995, *ApJ*, 445, 607
- Grebenev, S. A., Pavlinsky, M. N., & Sunyaev, R. A. 1995, *Proc. of the Workshop "Imaging in High Energy*
- Harrison, F. A., Craig, W. W., Christensen, F. E., et al. 2013, *ApJ*, 770, 103
- Inui, T., Koyama, K., Matsumoto, H., & Tsuru, T. G. 2009, *PASJ*, 61, 241
- Koyama, K., Maeda, Y., Sonobe, T., et al. 1996, *PASJ*, 48, 249
- Krivonos, R., Revnivtsev, M., Tsygankov, S., et al. 2010, *A&A*, 519, A107
- Law, C., & Yusef-Zadeh, F. 2004, *ApJ*, 611, 858
- Magdziarz, P., & Zdziarski, A. A. 1995, *MNRAS*, 273, 837
- Murakami, H., Koyama, K., Sakano, M., Tsujimoto, M., & Maeda, Y. 2000, *ApJ*, 534, 283
- Nowak, M. A., Neilsen, J., Markoff, S. B., et al. 2012, *ApJ*, 759, 95
- Ponti, G., Terrier, R., Goldwurm, A., Belanger, G., & Trap, G. 2010, *ApJ*, 714, 732
- Porquet, D., Rodriguez, J., Corbel, S., et al. 2003a, *A&A*, 406, 299
- Porquet, D., Predehl, P., Aschenbach, B., et al. 2003b, *A&A*, 407, L17
- Porquet, D., Grosso, N., Predehl, P., et al. 2008, *A&A*, 488, 549
- Predehl, P., Costantini, E., Hasinger, G., & Tanaka, Y. 2003, *Astronomische Nachrichten*, 324, 73
- Reis, R. C., Miller, J. M., Reynolds, M. T., et al. 2013, *ApJ*, 763, 48
- Revnivtsev, M. G., & Sunyaev, R. A. 2002, *Astronomy Letters*, 28, 19
- Revnivtsev, M. G., Churazov, E. M., Sazonov, S. Y., et al. 2004a, *A&A*, 425, L49
- Revnivtsev, M. G., Sunyaev, R. A., Varshalovich, D. A., et al. 2004b, *Astronomy Letters*, 30, 382
- Revnivtsev, M., Sazonov, S., Gilfanov, M., Churazov, E., & Sunyaev, R. 2006, *A&A*, 452, 169
- Rosati, P., della Ceca, R., Burg, R., Norman, C., & Giacconi, R. 1995, *ApJ*, 445, L11
- Ross, R. R., & Fabian, A. C. 2005, *MNRAS*, 358, 211
- Serabyn, E., Shupe, D., & Figer, D. F. 1998, *Nature*, 394, 448
- Slezak, E., Durret, F., & Gerbal, D. 1994, *AJ*, 108, 1996
- Starck, J.-L., & Murtagh, F. 1994, *A&A*, 288, 342
- Sunyaev, R., & Churazov, E. 1998, *MNRAS*, 297, 1279
- Sunyaev, R., & Kwant Team 1989, *IAU Circ.*, 4839, 1
- Sunyaev, R., Gilfanov, M., Churazov, E., et al. 1990, *Pisma v Astronomicheskii Zhurnal*, 16, 136
- Sunyaev, R. A., Markevitch, M., & Pavlinsky, M. 1993, *ApJ*, 407, 606
- Tatischeff, V., Decourchelle, A., & Maurin, G. 2012, *A&A*, 546, A88
- Terrier, R., Ponti, G., Bélanger, G., et al. 2010, *ApJ*, 719, 143

- Tsujimoto, M., Hyodo, Y., & Koyama, K. 2007, PASJ, 59, 229
- Vikhlinin, A., Forman, W., Jones, C., & Murray, S. 1995, ApJ, 451, 542
- Vikhlinin, A., Forman, W., & Jones, C. 1997, ApJ, 474, L7
- Vikhlinin, A., McNamara, B. R., Forman, W., et al. 1998, ApJ, 502, 558
- Vovk, I., Ferrigno, C., Drave, E. B. S. P., et al. 2012, The Astronomer's Telegram, 4381, 1
- Walter, R., Zurita Heras, J., Bassani, L., et al. 2006, A&A, 453, 133
- Wang, Q. D., Dong, H., & Lang, C. 2006, MNRAS, 371, 38
- Wijnands, R., Miller, J. M., Markwardt, C., Lewin, W. H. G., & van der Klis, M. 2001, ApJ, 560, L159
- Yusef-Zadeh, F., Law, C., Wardle, M., et al. 2002, ApJ, 570, 665
- Yusef-Zadeh, F., Muno, M., Wardle, M., & Lis, D. C. 2007, ApJ, 656, 847